Physica E 128 (2021) 114610

Contents lists available at ScienceDirect

Physica E: Low-dimensional Systems and Nanostructures

journal homepage: http://www.elsevier.com/locate/physe

Non-Fourier heat transport across 1D nano film between thermal reservoirs with different boundary resistances

S.L. Sobolev [a,c,*], Bing-Yang Cao [b], I.V. Kudinov [c]

[a] Institute of Problems of Chemical Physics, Academy of Sciences of Russia, Chernogolovka, Moscow Region, 142432, Russia
[b] Key Laboratory for Thermal Science and Power Engineering of Ministry of Education, Department of Engineering Mechanics, Tsinghua University, Beijing, 100084, China
[c] Samara State Technical University, ul. Molodogvardeiskaya 244, Samara, 443100, Russia

ARTICLE INFO

Keywords:
Nano film
Ballistic transport
Low-dimensional systems
Temperature jump
Effective thermal conductivity

ABSTRACT

We describe the nonlocal heat transport across a thin film in contact with two thermal baths using discrete variable model. The effective thermal conductivities, the boundary temperature jumps, the steady-state heat flux, and the internal temperature gradient are calculated analytically as functions of the film size and the boundary resistances. As the system size decreases, all the parameters demonstrate the transition from diffusive (Fourier) heat conduction when the scattering occurs mainly inside the film to ballistic transport when scattering occurs at the boundaries, while inside the film there is no scattering and the temperature profile is flat. We show that when the boundary resistance increases, the temperature profile inside the film also tends to be flat, but in this case the scattering, though small, occurs inside the film. The predicted effective thermal conductivity is consistent with classical continuous theories and available experimental data.

1. Introduction

Heat transfer mechanism at the nanoscale level has been of significant fundamental interest in the recent decade due to its practical importance for a large number of applications, ranging from thermoelectric devices for energy conversion to heat dissipation in thermal management [1–3]. Classical heat transfer description is based on the Fourier law $q = -\lambda\nabla T$, where q is the heat flux, λ the thermal conductivity and $\nabla T$the temperature gradient. Fourier law is local in space and is valid on a relatively large scale, which significantly exceeds the mean free path (MFP) of heat carriers. However, on the nanoscale level when the characteristic length is of the ordered of the MFP, the classical continuum theories reach their limits and fail to describe heat transport [1–16]. The recognition that a more detailed theoretical understanding of nanoscale heat transport than achievable using the Fourier law has lead to the development of approaches based on numerical solutions of the Boltzmann transport equation [2,3,9,17], microscopic Hamiltonian description of dissipative particle dynamics [8], Monte Carlo simulations [18,19], and molecular dynamic simulations (MD) [20–23]. The ballistic-diffusive approach [17–19,25–31], which divides the phonon intensity into ballistic and diffusive components, is also based on the Boltzmann transport equation. However, the approaches listed are usually cumbersome and computationally expensive methods are needed to obtain their solutions; thus, looking for simpler phenomenological models leading to reasonable predictions may be useful from the practical point of view as they offer a preliminary results, which may be refined later by means of cumbersome but more precise methods after having in a fast and efficient way the most promising physical conditions for the device operation. One of the most effective and relatively simple approaches to study heat transport on multi-length and -time scale including low-dimensional and sub-continuum regimes is the discrete variable model (DVM), which discretizes the transport process in space and time [4,12–14,32–36]. The DVM takes into account the fact that heat transport is an inherently nonlocal phenomenon because the heat flux at a point x depends on the history of the heat carriers reaching the point at time t and the carriers arrive at the point x having brought the energy from other points in space. The DVM provides a relatively simple but physically consistent framework of transport phenomena, which holds arbitrarily far from equilibrium and which is valid at the level of nano space scale. The steady-state heat transport across a nano film has been studied by the DVM with relatively simple boundary conditions between the film and the thermal baths [12]. The study correctly describes the temperature jumps at the boundaries, the temperature gradient inside the film, the heat flux and the effective thermal

* Corresponding author. Institute of Problems of Chemical Physics, Academy of Sciences of Russia, Chernogolovka, Moscow Region, 142432, Russia.
E-mail address: sobolev@icp.ac.ru (S.L. Sobolev).

https://doi.org/10.1016/j.physe.2020.114610
Received 25 September 2020; Received in revised form 15 December 2020; Accepted 28 December 2020
Available online 31 December 2020
1386-9477/

conductivities as functions of the film size. In this paper we analyze heat transport across a nano film with more general choice of coupling between the film and thermal reservoirs.

2. Model and results

2.1. Temperature jumps at the boundaries

Let us consider 1D heat conducting film divided into N discrete layers of equal size h parallel to the walls of thermal reservoirs. The temperatures of these discrete cells are determined by the discrete transfer equation [12,32–36]:

$$T_{n,j+1} = \frac{1}{2}\left(T_{n+1,j} + T_{n-1,j}\right) \tag{1}$$

where $T_{n,j}$ is the temperature of a discrete layer n at a discrete time moment j. For sake of simplicity the corresponding equations for the heat flux are presented for steady-state regime

$$q_{1,B1} = -\alpha_{B1}(T_1 - T_{B1}) \tag{2}$$

$$q_{n+1,n} = -Cv(T_{n+1} - T_n)/2 \tag{3}$$

$$q_{B2,N} = -\alpha_{B2}(T_{B2} - T_N) \tag{4}$$

where $q_{1,B1}$ is the heat fluxes between the left reservoir with temperature $T_{B1}$and the fist discrete layer of the system, $q_{n+1,n}$ is the heat flux between the discrete layers n and $n+1$inside the system, $q_{B2,N}$ is the heat flux between the right reservoir with temperature T_{B2} ($T_{B2} > T_{B1}$) and the last discrete layer $n = N$, N is the number of the discrete layers (see Fig. 1), α is the heat exchange coefficients between the neighboring subsystems, α_{B2} is the heat exchange coefficients between the system and the right reservoir, $\alpha_{1,B1}$ is the heat exchange coefficients between the system and the left reservoirs (thermal conductance per unit cross-sectional area), $C$is the specific heat, $v$is the group velocity of the heat carriers. Eqs. (2) and (4) describe the heat flux across the boundary between the regions with different thermal transport properties. The dissimilarity of the thermal transport properties of the regions in thermal contact leads to the boundary thermal resistance and boundary temperature jump [2,3,25]. The inverse of the heat exchange coefficients $R_K = 1/\alpha$ is also referred to as Kapitza resistance [2,3,25]. The definition for the heat current, Eq. (3), is a consequence of the continuity equation, which could be understood by noting that $CvT_{n+1}/2$ is simply the rate of energy flow from subsystem $n+1$ to subsystem n, and vice versa, and thus Eq. (3) describes the net energy flow between subsystems $n+1$ and n at the time moment t per unit time, i.e., the heat current. Assuming that the energy exchange between the neighboring subsystems is ballistic and the contacts between them are reflectionless, the heat exchange coefficient in Eq. (3) takes the form $\alpha = Cv/2$ [12].

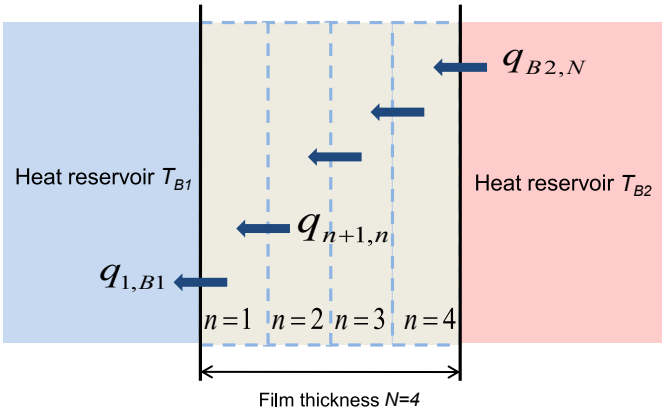

Fig. 1. Schematic representation of the model. The film, which consists of $N = 4$ layers, is placed between two thermal reservoirs with temperatures T_{B1} and T_{B2}, respectively. $q_{1,B1}$ is the heat fluxes between the left reservoir and the fist discrete layer $n = 1$, $q_{n+1,n}$ is the heat flux between the discrete layers n and $n+1$, $q_{B2,N}$ is the heat flux between the right reservoir with temperature and the last discrete layer $N = 4$.

The temperature difference between the thermal reservoirs $\Delta T = T_{B2} - T_{B1}$ can be expressed as

$$T_{B2} - T_{B1} = (N-1)\delta T + \delta T_{B2} + \delta T_{B1} \tag{5}$$

where δT_2 and δT_1 are the temperature jumps at the right and the left boundaries, respectively, δT is the temperature jump between the neighboring discrete subsystems. After some algebra, Eqs. (1)–(5) give

$$\delta T = \frac{T_{B2} - T_{B1}}{\frac{1}{\bar{\alpha}_2} + \frac{1}{\bar{\alpha}_1} - 1 + N} \tag{6}$$

where $\bar{\alpha}_1 = 2\alpha_{B1}/Cv$ and $\bar{\alpha}_2 = 2\alpha_{B2}/Cv$ are the nondimensional thermal conductances the left and the right boundary, respectively. In terms of the thermal conductivity $\lambda = Cvh/2$, the conductances take the form $\bar{\alpha}_1 = h\alpha_{B1}/\lambda$ and $\bar{\alpha}_2 = h\alpha_{B2}/\lambda$, respectively.

The temperature jumps at the boundaries are given by

$$\delta T_{B1} = \delta T/\bar{\alpha}_1 \tag{7}$$

$$\delta T_{B2} = \delta T/\bar{\alpha}_2 \tag{8}$$

In the Fourier regime $N \to \infty$ and Eqs. (6)–(8) give $\delta T_{B1} = \delta T_{B2} = 0$, as expected. In the ballistic limit $\delta T_{B1} + \delta T_{B2} = T_{B2} - T_{B1}$. In terms of the thermal resistances, Eqs. (6)–(8) can be rewritten as

$$\delta T = \frac{T_{B2} - T_{B1}}{R_{eff} + N} \tag{9}$$

$$\delta T_{B1} = \frac{(T_{B2} - T_{B1})R_1}{R_{eff} + N} \tag{10}$$

$$\delta T_{B2} = \frac{(T_{B2} - T_{B1})R_2}{R_{eff} + N} \tag{11}$$

where R_{eff} is the effective thermal resistance given by

$$R_{eff} = \frac{1}{\bar{\alpha}_1} + \frac{1}{\bar{\alpha}_2} - 1 \tag{12}$$

$R_1 = Cv/2\alpha_{B1}$ and $R_2 = Cv/2\alpha_{B2}$ are the nondimensional thermal resistances of the left and the right boundary, respectively. In terms of the thermal conductivity $\lambda = Cvh/2$, the conductances take the form $R_1 = \lambda/h\alpha_{B1}$ and $R_2 = \lambda/h\alpha_{B2}$, respectively. As the system size N increases, the temperature jumps decrease and tend to zero in the classical Fourier limit $N \to \infty$ when the heat transport is purely diffusive. When the system size N decreases, the ballistic component begins to play an important role, which leads to nonzero temperature jump at the boundaries. Taking into account that $R_{eff} = R_1 + R_2 - 1$ (see Eq. (12)) and summing up Eqs. (10) and (11), we obtain

$$\delta T_{B1} + \delta T_{B2} = \frac{(T_{B2} - T_{B1})(R_1 + R_2)}{R_{eff} + N} \tag{13}$$

In the ballistic limit, which in the DVM is reached at $N = 1$, Eq. (13) gives $(\delta T_{B1} + \delta T_{B2}) = (T_{B2} - T_{B1})$. This implies that in the ballistic limit the scattering occurs only at the boundaries.

If $R_1 \neq R_2$, Eqs. (10) and (11) give, $\delta T_{B1} \neq \delta T_{B2}$, which implies that the temperature profile inside the film is asymmetric. To discuss the asymmetry in more detail, we introduce the continuous temperature profile inside the film $T(x)$as follows

$$T(x) = T_{B1} + \delta T_{B1} + x(T_{B2} - T_{B1} - \delta T_{B1} - \delta T_{B2})/L \tag{14}$$

where x is the continuous coordinate ($+\,0 < x < L - 0$). Note that Eq.

(14) gives the temperature profile inside the film with $T(x) = T_{B1} + \delta T_{B1}$ at $x \to +0$ and $T(x) = T_{B2} - \delta T_{B2}$ at $x \to L-0$, whereas $T_{B1} = T(-0)$ and $T_{B2} = T(L+0)$, which implies temperature jumps at the boundaries in accordance with Eqs. (10) and (11). The situation is illustrated in Fig. 2, which depicts typical profiles of the nondimensional temperature $\theta(\xi) = (T(x) - T_{B1})/(T_{B2} - T_{B1})$ as a function of the nondimensional coordinate $\xi = x/L$ for different values of the boundary resistances. When $N \to \infty$, Eqs. (10) and (11) give that $\delta T_{B1} = \delta T_{B2} \to 0$ independently of the boundary resistance, which corresponds to the classical Fourier diffusive limit when scattering occurs mainly in the bulk system, while the boundary scattering is negligible (see the dashed line in Fig. 2). When N decreases, the boundary scattering begins to play an important role and the boundary temperature jumps appear. If $R_1 = R_2$, Eqs. (10) and (11) give $\delta T_{B1} = \delta T_{B2}$, i.e. the temperature profile is symmetric (see dash-dotted curve in Fig. 2). In such a case the scattering occurs both at the boundaries and inside the system, i.e. the transport is both ballistic and diffusive. When $R_1 \neq R_2$, the temperature jumps at the boundaries are different ($\delta T_1 \neq \delta T_2$) and the temperature profile is asymmetric (see solid line with $\delta T_{B1} > \delta T_{B2}$ and grey line with $\delta T_{B1} < \delta T_{B2}$ in Fig. 2). Note that the temperature gradients inside the film for temperature profiles depicted by solid and dash-dotted lines in Fig. 2 are the same, while the temperature jumps at the boundaries are different. If $R_2 \to \infty$, which implies that the right boundary is adiabatically isolated, Eqs. 9–11 give $\delta T \to 0$ and $\delta T_1 \to 0$, whereas $\delta T_2 \to (T_{B2} - T_{B1})$. In such a case, the steady-state heat flux through the film is small and the temperature is close to T_{B1} (see grey curve in Fig. 2). The scattering occurs mainly at the right boundary, which is manifested by high temperature jump at the right boundary in comparison with the temperature jump the left boundary $\delta T_{B2} >> \delta T_{B1}$ and small temperature gradient inside the film. In the opposite limit of small thermal resistance $R_{B2} \to 0$, the corresponding temperature jump tends to zero and scattering occurs mainly in the bulk system and at the left boundary. Thus the asymmetry of the temperature profile (solid and grey lines in Fig. 2) arises due to different values of the boundary resistance between the system and the reservoirs.

Fig. 3 shows the nondimensional temperature $\theta(\xi)$ as a function of the nondimensional coordinate $\xi = x/L$ at $R_1/R_2 = 2$ and for different values of the system size $N = L/h$. When $N \to \infty$, the scattering occurs

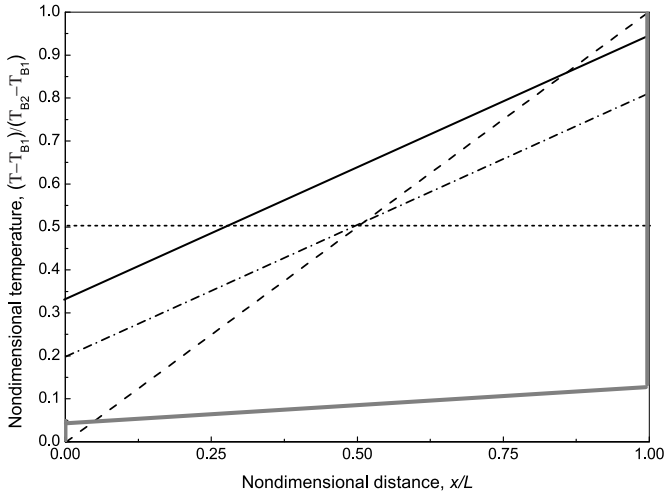

Fig. 2. Nondimensional temperature profiles across a thin film $\theta(\xi)$, obtained from Eq. (14), as a function of the nondimensional coordinate $\xi = x/L$ for different values of the boundary resistances. Thick grey curve corresponds to nearly adiabatic right boundary with high resistance $R_2 \to \infty$, which implies that most of the scattering occurs at the boundary with high temperature jump $\delta T_{B2} \to (T_{B2} - \delta T_{B1})$, while both the temperature jump at the left boundary and the temperature gradient inside the film tend to zero. Solid curve - ballistic-diffusive regime with asymmetric temperature profile due to $R_1 > R_2$. Dash-dotted curve - ballistic-diffusive regime with symmetric temperature profile ($R_1 = R_2$). Dashed curve – classical Fourier (diffusive) limit $N \to \infty$.

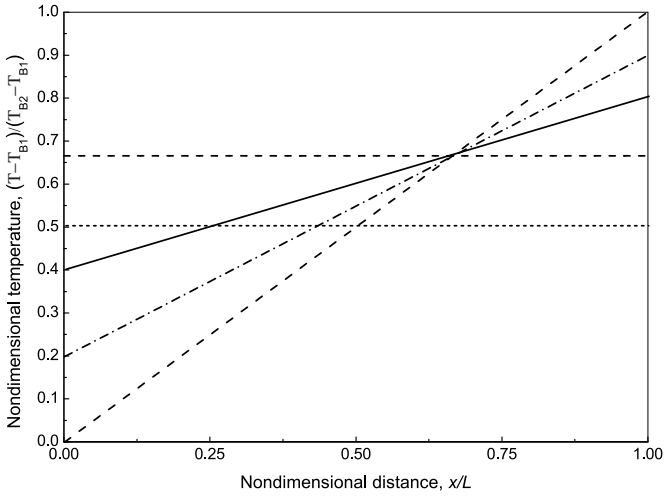

Fig. 3. Nondimensional temperature across a thin film $\theta(\xi)$, obtained from Eq. (14), as a function of the nondimensional coordinate $\xi = x/L$ at $R_1/R_2 = 2$ and for different values of the film size $N = L/h$. Fourier (diffusive) limit $N \to \infty$: dashed line. Scattering occurs only inside the film and leads to the maximum temperature gradient inside the film, while $\delta T_{B2} = \delta T_{B1} = 0$. Ballistic limit - horizontal lines. Dashed line for $R_1/R_2 = 2$; short-dashed line for $R_1 = R_2$. Scattering occurs only at the boundaries with $\delta T_{B1} + \delta T_{B2} = T_{B2} - T_{B1}$, while temperature gradient inside the film is zero. At the intermediate values of the system size N (ballistic-diffusive regime) the scattering occurs both at the boundaries (nonzero temperature jumps) and inside the film (nonzero temperature gradient inside the film): solid curve $R_1/(R_{eff} + N) = 0.4$ and dash-dotted curve $R_1/(R_{eff} + N) = 0.2$.

only inside the film and one obtains the symmetrical Fourier profile with $\delta T_{B2} = \delta T_{B1} = 0$ (see dashed line in Fig. 3). In the opposite limit, the scattering occurs only at the boundaries, while the temperature prolife inside the film is flat (see horizontal dashed line in Fig. 3 and compare it with horizontal dotted line, which depicts ballistic temperature profile for $R_1 = R_2$). At the intermediate values of the system size N, the scattering occurs both at the boundaries and inside the film, which is manifested by nonzero temperature jumps at the boundaries ($\delta T_{B2} \neq \delta T_{B1}$) and nonzero temperature gradient inside the film (see solid lines in Fig. 3).

In the center of the film at $x/L = 1/2$, Eq. (14) gives $T(L/2) = (T_{B2} + T_{B1})/2 + (\delta T_{B1} - \delta T_{B2})/2$.

This implies that when $R_1 \neq R_2$ and, hence, $\delta T_{B1} \neq \delta T_{B2}$, the temperature in the center of the film $T(L/2)$ is not equal to the temperature $T_F = (T_{B2} - T_{B1})/2$due to the applied Fourier temperature gradient (see Fig. 3). Note that the ratio $\delta T_{B1}/\delta T_{B2} = R_1/R_2$ is independent of the film size and all the temperature profiles $T(x)$ crosses over with the ballistic profile at the same point (see Fig. 3). However, the difference $\delta T_{B1} - \delta T_{B2} = \frac{(T_{B2} - T_{B1})(R_1 - R_2)}{R_1 + R_2 + N - 1}$decreases with increasing system size N, and the temperature profile tends to the classical symmetric Fourier profile (see Fig. 3).

The temperature gradient inside the film is given by $\nabla T = (T(L-0) - T(+0))/L$, where $T(L-0) = T_{B2} - \delta T_{B2}$ and $T(+0) = T_{B1} + \delta T_{B1}$. Using Eqs. (10) and (11), we obtain

$$\nabla T = \frac{(T_{B2} - T_{B1})}{L} \frac{N-1}{R_{eff} + N} \tag{15}$$

The first multiplier on the right hand side of Eq. (15) represents the imposed temperature gradient, while the second multiplier is the non-local correction. When $N \to \infty$, the non-local correction tends to unity and Eq. (15) reduces to the imposed temperature gradient inside the film with zero temperature jumps at the boundaries. As the film size N decreases, the nonlocal correction and, consequently, the temperature gradient inside the film ∇T, Eq. (15), begin to decrease. When $N = 1$, Eq. (15) gives $\nabla T = 0$, i.e. the purely ballistic regime with flat

temperature profile is reached. It should be stressed that the flat temperature profile can be reached not only in the ballistic limit with decreasing system size N, but also with increasing total boundary resistance. Indeed, when $R_{eff}\to\infty$, Eq. (13) gives $(\delta T_{B1}+\delta T_{B2})\to(T_{B2}-T_{B1})$, while Eq. (15) gives $\nabla T\to 0$, which implies that the scattering occurs mainly at the boundaries, whereas the scattering inside the system is relatively small. Thus, at high total boundary resistance $R_{eff}\to\infty$, the temperature profile tends to be flat independently of the film size.

Using Eqs. (3) and (9), we obtain the steady-state heat flux as follows

$$q=-\frac{Cv}{2}\frac{T_{B2}-T_{B1}}{R_{eff}+N} \tag{16}$$

When $N\to\infty$, Eq. (16) gives $q=-Cvh(T_{B2}-T_{B1})/2L$. Taking into account that for 1D case $\lambda=Cvh/2$, the last equation represents the classical Fourier law $q=-\lambda(T_{B2}-T_{B1})/L$. In the ballistic $N\to 1$, Eq. (16) gives $q=-Cv(T_{B2}-T_{B1})/2R_{eff}$. For an intermediate value of the film size N when the transport is both ballistic and diffusive, it is convenient to represent Eq. (16) in the form

$$q=-\frac{\lambda(T_{B2}-T_{B1})}{L}\frac{N}{R_{eff}+N} \tag{17}$$

The first multiplier on the right hand side of Eq. (17) is the classical Fourier law, while the second one is the nonlocal correction, which reflects the ballistic component of the heat transport. To analyze the dependence of the heat flux q on the film size N, we consider two cases. The first one assumes that the imposed temperature gradient $(T_{B2}-T_{B1})/L$ is kept constant. In such a case Eq. (17) gives

$$|q_1|=\frac{N}{R_{eff}+N} \tag{18}$$

where q_1 is the heat flux q scaled with $\lambda(T_{B2}-T_{B1})/L$. The second case assumes that the temperature difference between the baths $(T_{B2}-T_{B1})$ is kept constant. In this case Eq. (17) reduces to

$$|q_2|=\frac{1}{R_{eff}+N} \tag{19}$$

where q_2 is the heat flux q, scaled with $\lambda(T_{B2}-T_{B1})/h$. Eqs. (18) and (19) demonstrate that the dependence of the heat flux q on the system size N is governed by the external conditions. When $N\to\infty$, the heat flux $|q_1|$ at constant imposed temperature gradient, Eq. (18), tends to unity, whereas the heat flux $|q_2|$ at constant temperature difference between thermal baths, Eq. (19), tends to zero. As the system size decreases, $|q_1|$ decrease, while $|q_2|$ tends to a finite value $1/R_{eff}$. Note that when $R_{eff}\to\infty$ both $|q_1|$ and $|q_2|$ tend to zero as $1/R_{eff}$. Fig. 4 shows $|q_1|$, Eq. (18), and $|q_2|$, Eq. (19), as functions of the system size for different values of the total boundary resistance R_{eff}.

Eq. (17) allows us to introduce an effective thermal conductivity λ_{eff}, which virtually keeps the constitutive equation for the heat flux in the classical Fourier law $q=-\lambda_{eff}(T_{B2}-T_{B1})/L$, as follows

$$\frac{\lambda_{eff}}{\lambda}=\frac{1}{1+R_{eff}/N} \tag{20}$$

Fig. 5 shows the effective thermal conductivity, Eq. (20), as a function of the system size N for different values of the total boundary resistance R_{eff}. In the Fourier limit $N\to\infty$, Eq. (20), as expected, gives $\lambda_{eff}\to\lambda$, whereas in the ballistic limit we obtain $\lambda_{eff}\to\lambda_{ball}=\lambda N/R_{eff}$.

The effective thermal conductivity λ_{eff}, Eq. (20), corresponds to the Fourier law in terms of the imposed temperature gradient $(T_{B2}-T_{B1})/L$. However, one can define an effective thermal conductivity λ^{∇}_{eff}, which keeps the classical form of the Fourier law in terms of the internal temperature gradient ∇T, Eq. (15) [12]. Using Eqs. (15) and (17), we obtain

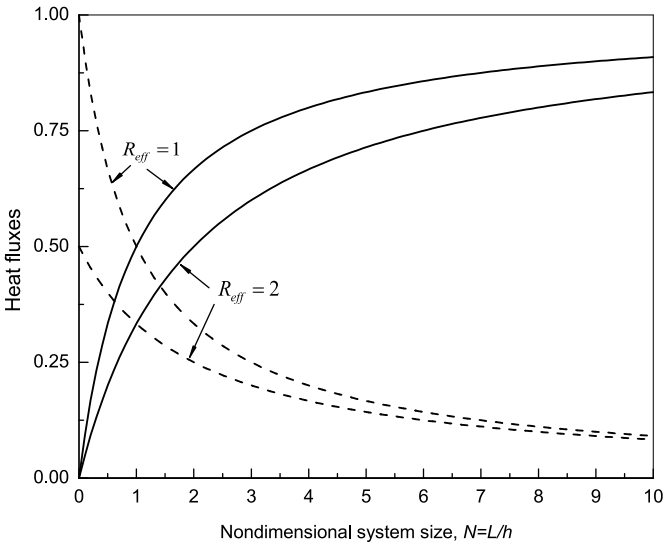

Fig. 4. Heat flux $|q_1|$ at constant imposed temperature gradient, Eq. (18), and heat flux $|q_2|$ at constant temperature difference between thermal baths, Eq. (19), as functions of the system size N for different values of the total boundary resistance R_{eff} - solid and dashed lines, respectively.

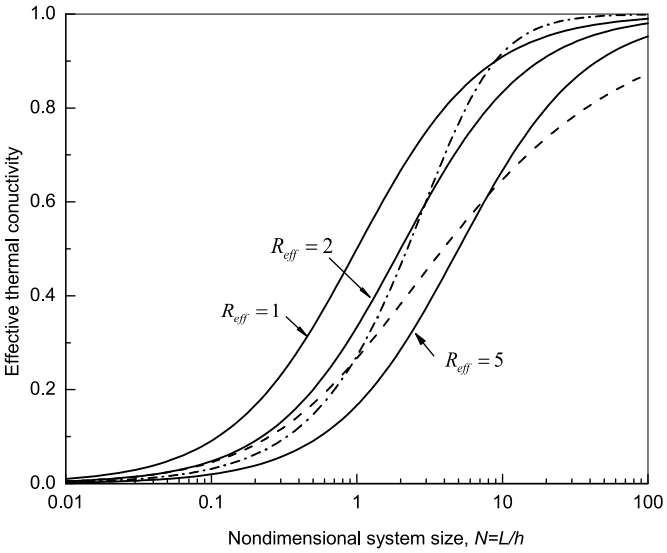

Fig. 5. Effective thermal conductivity λ_{eff}, scaled with bulk thermal conductivity λ, Eq. (20), as a function of the system size N for different values of the total boundary resistance R_{eff} (solid lines). Dash-dotted line – effective thermal conductivity λ_{EIT}, Eq. (23), due to EIT [3,24]. Dashed line - effective thermal conductivity k_{C-P}, Eq. (24), obtained by McGaughey et al. [39].

$$\frac{\lambda^{\nabla}_{eff}}{\lambda}=\frac{N}{N-1} \tag{21}$$

In the Fourier limit $N\to\infty$, the effective thermal conductivity in terms of the internal temperature gradient λ^{∇}_{eff}, Eq. (21), as well as the effective thermal conductivity in terms of the internal temperature gradient λ_{eff}, Eq. (20), tend to the bulk value λ. However, they behave differently when the film size ℓ decreases, namely, while λ_{eff}, Eq. (20), decreases, λ^{∇}_{eff}, Eq. (21), increases. The increase of λ^{∇}_{eff}, Eq. (21), with decreasing film size keeps a finite value of the heat flux compensating vanishing internal temperature gradient, Eq. (15). Note that λ^{∇}_{eff}, Eq. (21), does not depend on the boundary resistance R_{eff}, whereas λ_{eff}, Eq. (20), depends.

3. Discussion and comparison with other theories

3.1. Temperature profiles

We start the discussion by comparison with the MD simulation of Tenenbaum et al. [21], which studied 1D nonequilibrium steady-state heat conduction between two thermal reservoirs. The method was based on the introduction of stochastic boundary conditions and was able to simulate high temperature gradients in a region of dense fluids ranging from the gas-liquid coexistence line to the freezing line. The main result of the MD simulations, namely, the different temperature jumps at the right and the left boundaries, corresponds to the prediction of the present model, Eqs. 9–11 (compare Fig. 3 in this paper with Fig. 3 in Ref. [21]). Another manifestation of the asymmetry of the temperature profile is the difference between the temperatures of the applied and obtained gradients at the center of the film, which has been observed both in the present model (see Fig. 3) and in the MD simulation (see Fig. 3 in Ref. [21]). Moreover, the MD simulation of Tenenbaum et al. [21] predicts that the temperature jumps at the boundaries increase linearly with the temperature difference between the thermal baths ΔT, and that δT_R is always greater than δT_L, for a given gradient. These results are also in agreement with the present model (see Eqs. (10) and (11)).

Shiomi and Maruyama [22] studied heat conduction of finite-length single-walled carbon nanotubes by means of nonequilibrium MD dynamics simulations. The Nose–Hoover thermostats with two tuning parameters, namely, the length of the temperature-controlled part and the relaxation time, have been used. The MD simulations demonstrate that the shorter the length of the temperature-controlled part of the nanotube, the higher the temperature jumps at the boundaries. Moreover, the calculated temperature profile is asymmetrical - the temperature jump at the high temperature boundary exceeds the temperature jump at the low temperature boundary [22]. The asymmetry increases with decreasing temperature-controlled part. For instance, when the temperature-controlled part $L_c$is equal to $0.01L$, the temperature jump at the low temperature boundary is 5K, whereas at the high temperature boundary is 10K, i.e. the temperature jump at the higher temperature boundary is twice as much as the temperature jump at the low temperature boundary. The sum of the temperature jumps account for about 75% of temperature difference between the reservoirs, which is equal to 20K.

The MD simulation of Jiang et al. [23] studied the boundary temperature jumps in a graphene nanoribbon consisting of 51 atomic columns. Application of Nośe-Hoover heat baths to columns 2 and 50 with temperatures 310 and 290 K, respectively, gives the same values of the boundary temperature jumps as in Ref. [22] at $L_c = 0.01L$. These results correspond to present model (compare the dashed curve in Fig. 3 in this paper with the blue curve in Fig. 2 of Ref. [22] and with the red dotted curve in Fig. 6a of Ref. [23]).

Recently, using nonequilibrium molecular dynamic (NEMD) simulations, Feng et al. [20] observed the local thermal nonequilibrium between the ballistic and diffusive phonons, which provides a significant additional thermal interfacial resistance mechanism besides phonon reflection. The NEMD simulations of Feng et al. [20] demonstrated asymmetric temperature profiled in thin films (see, for example, Fig. 4c in Ref. [20]).

3.2. Effective thermal conductivity

Classical continuous approaches to the heat transport in nano films provide the effective (size-dependent) thermal conductivity across a thin film as follows [2,3,8,12,38].

$$\frac{\lambda_{eff}^{\varepsilon}(N)}{\lambda} = \frac{1}{1+2\varepsilon/N} \tag{22}$$

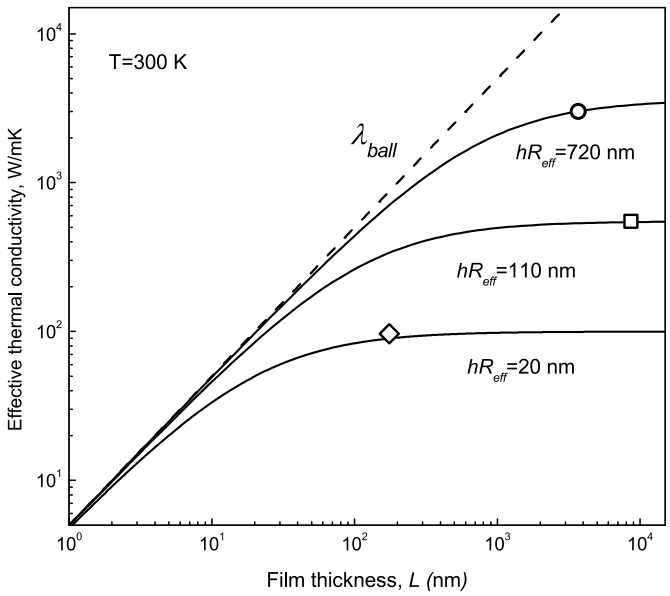

Fig. 6. Effective thermal conductivityλ_{eff}, Eq. (20), as a function of film thickness L for different values of h. The dashed line is the ballistic limit $\lambda_{ball} = \lambda L/hR_{eff}$, solid lines represent λ_{eff} calculated with hR_{eff} = 720nm, hR_{eff} = 110nm, and hR_{eff} = 20nm chosen to match existing experimental data for suspended graphene, supported graphene, and graphene nanoribbons, respectively [10].

ε is a constant corresponding to the efficacy of the boundary thermal baths as they couple to the system (coupling parameter). Eq. (20) corresponds to Eq. (21) at $\varepsilon = R_{eff}/2$. The Matthiessen rule with allowance for the concept of size-dependent (effective) mean free path of energy carriers [2], as well as the simples version of the DVM [12], give $\varepsilon = 1/2$ (see the upper dotted line in Fig. 6). Majumbar [9] obtained $\varepsilon = 2/3$ on the basis of the relaxation time approximation to the BTE. Noted that this approximation assumes that the distribution function is not too far away from equilibrium, i.e. the process occurs under local-equilibrium conditions. Strictly speaking, when $L \sim h$, the ballistic component of heat transport begins to play an important role, which implies that there is no local equilibrium. This may lead to some error in the effective thermal conductivity [9].

The FPU-β model for the effective thermal conductivity in nano film [8,37] implies that the coupling parameter ε vary from $\varepsilon = 0.8$ for the thermostats adopted in Ref. [37] (demons), to $\varepsilon = 2$ for Nose-Hoover thermostats [8,37] and to ε = 40for stochastic reservoirs [8]. The transition of thermal conductivity from the ballistic to the diffusive regime can be also approximated through a Landauer-like approach, which gives $\varepsilon = 1/\pi$ [38]. Extended irreversible thermodynamics, which describes local nonequilibrium systems by introducing additional state variables, such as heat flux, gives the following expression for the size-dependent thermal conductivity for 1D systems [3,24].

$$\lambda_{EIT}\left(N\right) = \frac{3\lambda N^2}{4\pi^2}\left(\frac{2\pi}{N\arctan(2\pi/N)} - 1\right) \tag{23}$$

Fig. 5 shows λ_{EIT}, Eq. (23), as a function of N (see dash-dotted line). McGaughey et al. [39] calculated the in-plane and cross-plane effective thermal conductivities by including the mode-dependence of the phonon lifetimes resulting from phonon-phonon and phonon-boundary scattering. Using the Matthiessen rule and the Debye approximation for the phonon dispersion, which assumes a single acoustic branch, the cross-plane effective thermal conductivity takes the form [39].

$$\frac{k_{C-P}(\ell)}{\lambda} = \frac{6}{7} + \frac{3}{14}\ell - \frac{3}{7}\ell^2 + \frac{3}{7}\ell^3\ln\left(1+\frac{1}{\ell}\right) - \frac{6}{7\sqrt{\ell}}\arctan\sqrt{\ell} \tag{24}$$

where ℓ is a non-dimensional length defined as $\ell = 3k_B v_{ac} L/\, 2\lambda\Omega$, where Ω is the primitive cell volume, $v_{ac}$is the acoustic velocity, $k_B$is the Boltzmann constant. For silicon, which has a diamond structure, the primitive cell volume is $a^3/4$, where a is the lattice constant. Taking into account that for 1D system $\lambda = Cvh/2$, ℓcan be expressed as $N = C_\infty L/2Ch$, where C_∞ is the high-temperature harmonic specific heat [39]. Assuming that $C_\infty \approx C$, one obtains $\ell \approx N/2$. Fig. 5 shows k_{C-P}, Eq. (24), as a function of N (see dashed line).

The effective thermal conductivityλ_{eff}, Eq. (20), is shown in Fig. 6 as a function of the film thickness L for different values of hR_{eff} : $hR_{eff} =$ 720nm, $hR_{eff} =$ 110nm, and $hR_{eff} =$ 20nm chosen to match existing experimental data for suspended graphene, supported graphene, and graphene nanoribbons, respectively [10]. The dashed line is the ballistic limit $\lambda_{ball} = \lambda L/hR_{eff}$, which is obtained from Eq. (20) in the limit small film thickness. The predicted effective thermal conductivity λ_{eff}, Eq. (20), is consistent with the classical continuous theoretical approaches, Eqs.22–24, (see Fig. 5) and available experimental data (see Fig. 6).

4. Conclusion

The discrete variable model takes into account the fundamental role of the time and length scales in the heat transport. This is particularly important for the performance evaluation of modern thermal nano systems and microdevices, which usually operate under extreme conditions. The model is used to study heat conduction across a thin film between two thermal baths, which have different thermal boundary resistances with the film. The effective thermal conductivities, the boundary temperature jumps, the steady-state heat flux, the internal temperature gradient are obtained analytically and analyzed as functions of the film size and boundary resistances. As the system size decreases, all these parameters demonstrate the crossover from diffusive to ballistic behavior. Moreover, as the total boundary resistance increases, the temperature profile inside the film tends to be flat, while the total boundary temperature jump reaches the imposed temperature difference between the baths. In such a case the scattering inside the film is relatively small in comparison with the scattering at the boundaries. The predicted effective thermal conductivity is consistent with the classical continuous treatments and available experimental data. The results are given in a relatively simple analytical form and can be easily implemented for practical experimental conditions or used as an effective tool for rapid calculations to make more elaborated approaches less computationally expensive.

Declaration of competing interest

The authors declare that they have no known competing financial interests or personal relationships that could have appeared to influence the work reported in this paper.

Acknowledgments

The reported study was funded by RFBR and NSFC according to the research project # 20-58-53017. This work was performed as a part of the State Task, State Registration AAAA-A19-119071190017-7.

References

[1] Jesko Sirker, Physics at the nanoscale special issue in honor of Tapash Chakraborty, Phys. E Low-dimens. Syst. Nanostruct. 117 (2020) 113858, https://doi.org/10.1016/j.physe.2019.113858.
[2] Z.M. Zhang, Nano/Microscale Heat Transfer, McGraw-Hill Professional, New York, 2007.
[3] H. Machrafi, Extended Non-equilibrium Thermodynamics: from Principles to Applications in Nanosystems, CRC Press, Taylor & Francis, 2019.
[4] I.V. Andrianov, J. Awrejcewicz, D. Weichert, Improved continuous models for discrete media, Math. Probl Eng. 2010 (2010) 1–35, https://doi.org/10.1155/2010/986242.
[5] S.I. Serdyukov, Macroscopic entropy of non-equilibrium systems and postulates of extended thermodynamics: application to transport phenomena and chemical reactions in nanoparticles, Entropy 20 (2018) 802–819.
[6] M.F. Ben Aissa, H. Rezgui, F. Nasri, H. Belmabrouk, A. Guizani, Thermal transport in graphene field-effect transistors with ultrashort channel length, Superlattice. Microst. 128 (2019) 265–273, https://doi.org/10.1016/j.spmi.2019.02.004.
[7] W. Liu, K. Saanouni, S. Forest, P. Hu, The micromorphic approach to generalized heat equations, J. Non-Equilibr. Thermodyn. 42 (2017) 327–358, https://doi.org/10.1515/jnet-2016-0080.
[8] S. Lepri, R. Livi, A. Politi, Thermal conduction in classical low-dimensional lattices, Phys. Rep. 377 (2003) 1–80.
[9] A. Majumdar, Microscale heat conduction in dielectric thin films, J. Heat Tran. 115 (1993) 7–16.
[10] E. Pop, V. Varshney, A.K. Roy, Thermal properties of graphene: fundamentals and applications, MRS Bull. 37 (2012) 1273–1281.
[11] M. Xu, A non-local constitutive model for nano-scale heat conduction, Int. J. Thermal Sciences 134 (2018) 594–600.
[12] S.L. Sobolev, Discrete space-time model for heat conduction: application to size dependent thermal conductivity in nano-films, Int. J. Heat Mass Tran. 108 (2017) 933–939, https://doi.org/10.1016/j.ijheatmasstransfer.2016.12.051.
[13] I. Carlomagno, A. Sellitto, V.A. Cimmelli, Phonon-electron coupling and nonlocal heat transport in Bi2Te3 nanowires, Phys. E Low-dimens. Syst. Nanostruct. 108 (2019) 421–427.
[14] S.L. Sobolev, Space-time nonlocal model for heat conduction, Phys. Rev. E 50 (1994) 3255–3258, https://doi.org/10.1016/j.ijheatmasstransfer. 2013.12.048.
[15] S.L. Sobolev, Nonlocal two-temperature model: application to heat transport in metals irradiated by ultrashort laser pulses, Int. J. Heat Mass Tran. 94 (2016) 138–144, https://doi.org/10.1016/j.ijheatmasstransfer.2015.11.075.
[16] M.G. Hennessy, M. Calvo-Schwarzwälder, T.G. Myers, Modelling ultra-fast nanoparticle melting with the Maxwell–Cattaneo equation, Appl. Math. Model. 69 (2019) 201–222, https://doi.org/10.1016/j.apm.2018.12.004.
[17] G. Chen, Ballistic-diffusive equations for transient heat conduction from nano to macroscales, ASME J. Heat Transfer 124 (2002) 320–328.
[18] H.-L. Li, Y.-C. Hua, B.-Y. Cao, A hybrid phonon Monte Carlo-diffusion method for ballistic-diffusive heat conduction in nano- and micro- structures, Int. J. Heat Mass Tran. 127 (2018) 1014–1022.
[19] Y.C. Hua, B.Y. Cao, Phonon ballistic-diffusive heat conduction in silicon nanofilms by Monte Carlo simulations, Int. J. Heat Mass Tran. 78 (2014) 755–759.
[20] T. Feng, W. Yao, Z. Wang, J. Shi, C. Li, B. Cao, X. Ruan, Spectral analysis of nonequilibrium molecular dynamics: spectral phonon temperature and local nonequilibrium in thin films and across interfaces, Phys. Rev. B 95 (2017) 195202–195213.
[21] A. Tenenbaum, G. Ciccotti, R. Gallico, Stationary nonequilibrium states by molecular dynamics. Fourier's law, Phys. Rev. A 25 (1982) 2778–2787.
[22] J. Shiomi, S. Maruyama, Molecular dynamics of diffusive-ballistic heat conduction in single-walled carbon nanotubes, Jpn. J. Appl. Phys. 47 (2008), 2005–2009.
[23] J.-W. Jiang, J. Chen, J.-S. Wang, B. Li, Edge states induce boundary temperature jump in molecular dynamics simulation of heat conduction, Phys. Rev. B 80 (2009) 52301–52304.
[24] H. Machrafi, Temperature distribution through a nanofilm by means of a ballistic-diffusive approach, Inventions 4 (2019) 2.
[25] Y. Dong, B.-Y. Cao, Z.-Y. Guo, Ballistic–diffusive phonon transport and size induced anisotropy of thermal conductivity of silicon nanofilms, Physica E 66 (2015) 1–6.
[26] H. Rezgui, F. Nasri, M.F. Ben Aissa, H. Belmabrouk, A.A. Guizani, Modeling thermal performance of nano-GNRFET transistors using ballistic-diffusive equation, IEEE Trans. Electron. Dev. 65 (2018) 1611–1616, https://doi.org/10.1109/TED.2018.2805343.
[27] A. Famà, L. Restuccia, P. Ván, Generalized ballistic-conductive heat transport laws in three-dimensional isotropic materials, Continuum Mech. Therm. (2020), https://doi.org/10.1007/s00161-020-00909-w.
[28] H.L. Li, B.Y. Cao, Radial ballistic diffusive heat conduction in nanoscale, Nanoscale Microscale Thermophys. Eng. 23 (2019) 10–24.
[29] Y.C. Hua, B.Y. Cao, Slip boundary conditions in ballistic diffusive heat transport in nanostructures, Nanoscale Microscale Thermophys. Eng. 21 (2017) 159–176.
[30] D.S. Tang, B.Y. Cao, Superballistic characteristics of transient phonon ballistic-diffusive conduction, Appl. Phys. Lett. 111 (2017) 113109.
[31] Y.C. Hua, B.Y. Cao, Ballistic-diffusive heat conduction in multiply constrained nanostructures, Int. J. Therm. Sci. 101 (2016) 126–132.
[32] Ya B. Zeldovich, A.D. Myskis, Elements of Mathematical Physics, Nauka, Moscow, 1973.
[33] S.L. Sobolev, Discrete model for transfer processes, Phys. Lett. A 163 (1992) 101–103.
[34] S.L. Sobolev, Two-temperature discrete model for nonlocal heat conduction, J. Phys. III France 3 (1993) 2261–2269.
[35] S.L. Sobolev, Local non-equilibrium transport models, Phys. Usp. 40 (1997) 1043–1053.
[36] S.L. Sobolev, Nonlocal diffusion models: application to rapid solidification of binary mixtures, Int. J. Heat Mass Tran. 71 (2014) 295–302.
[37] K. Aoki, D. Kusnezov, Fermi-pasta-ulam β model: boundary jumps, fourier's law, and scaling, Phys. Rev. Lett. 86 (2001) 4029–4032.
[38] R. Prasher, Thermal boundary resistance and thermal conductivity of multiwalled carbon nanotubes, Phys. Rev. B 77 (2008) 75424.
[39] A.J.H. McGaughey, E.S. Landry, D.P. Sellan, C.H. Amon, Size-dependent model for thin film and nanowire thermal conductivity, Appl. Phys. Lett. 99 (2011) 131904.